Dynamic Indentation of an Elastic-Plastic Multi-Layered Medium by a Rigid Cylinder

J. Yang, Graduate Student

K. Komvopoulos, Professor (Fellow ASME)

Department of Mechanical Engineering
University of California
Berkeley, CA 94720

Abstract

A plane-strain analysis of dynamic indentation of an elastic-plastic multi-layered medium by a rigid cylinder was performed using the finite element method. Conversely to plane-strain static contact analysis, the solutions of dynamic contact analysis within a given subsurface domain adjacent to the contact region are independent of the mesh size, provided it is sufficiently large such that the time required for propagating waves to be reflected from the artificial boundaries back into the analyzed domain to be greater than the analysis time. Simulation results for the normal force, contact pressure distribution, subsurface stresses, and evolution of plasticity in the multi-layered medium are presented in terms of the speed and radius of the rigid indenter. The likelihood of mechanical failure due to excessive plastic deformation and cracking is interpreted in terms of finite element results for the von Mises equivalent stress, first principal stress, and equivalent plastic strain obtained for different values of the indenter speed and radius of curvature.

Submitted to the ASME *Journal of Tribology* on February 28, 2003.

1. Introduction

Hard and tough surface layers are traditionally used in engineering components to improve the contact fatigue resistance and tribological properties of interacting surfaces and to protect the substrate medium from the accumulation of inelastic deformation and the occurrence of cracking. Fundamental knowledge of the stress and strain fields in layered media subjected to surface traction is critical to the endurance of electromechanical devices undergoing repetitive contact, such as relays, switches, vibromotors, and micromirror displays. Early studies dealing with normal contact of layered media provided analytical treatments for the elastic response due to indentation loading. Burmister (1945) obtained solutions for the stresses and displacements in an elastic single-layered medium subjected to axisymmetric surface loading. Dhaliwal and Rau (1970) obtained a solution for the axisymmetric Boussinesq problem of an elastic layer on an elastic foundation. Gupta and Walowit (1974) developed a plane-strain elastic theory for a layered medium under both normal and tangential surface loadings. King and O'Sullivan (1987) extended the previous theory to obtain analytical solutions for an elastic layered medium under sliding contact loading. Brock and Georgiadis (1994) presented a dynamic analysis of a linear-elastic half-plane indented by either a wedge or a parabolic rigid indenter.

Despite valuable insight into the mechanics of indented media derived from previous analytical studies, it is difficult to apply the approaches of these works to the analysis of elastic-plastic contact of layered media. Consequently, numerical techniques based mainly on the finite element method were advanced to deal with more complicated contact geometries and more realistic constitutive laws. One of the first finite element analysis of elastic-plastic indentation of layered media is attributed to Kennedy and Ling (1974) who investigated the effects of layer thickness, mechanical properties of the layer and substrate materials, and interfacial contact

conditions on plastic deformation in the layered medium. Komvopoulos (1989) investigated the plane-strain problem of a rigid cylinder indenting an elastic-plastic substrate coated with a harder and stiffer layer using the finite element method. Plastic deformation was found to initiate at the layer/substrate interface and the contact pressure profile was significantly flattened with increasing plastic deformation. In a finite element analysis of an elastic-plastic layered medium penetrated by an elastic indenter performed by Montmitonnet et al. (1993) the stress field in the layered medium was interpreted in terms of the layer thickness, and the highest tensile stress was reported to occur at the surface of the medium. Kral et al. (1995a, 1995b) presented a finite element contact analysis of a layered medium exhibiting either perfectly plastic or isotropic strain hardening post-yield behavior repeatedly indented by a rigid sphere and interpreted the propensity for crack initiation during the first indentation cycle in the context of the obtained finite element results.

More recently, Gan and Ben-Nissan (1997) examined the influence of the mechanical properties of a ductile substrate coated with a hard layer on the indentation load and reported a significant effect of the yield strength and strain hardening properties and a minor effect of the elastic modulus on the applied normal load. Faulkner et al. (1998) compared finite element results for an elastic-plastic layered medium in contact with a rigid or deformable indenter and observed higher contact pressures in the elastic regime and lower peak radial tensile stress in the case of the rigid indenter. Sen et al. (1998) used the finite element technique to model indentation of an elastic-work hardening layered medium by an elastic sphere and obtained elastic and elastic-plastic solutions for the contact pressure distribution. Souza et al. (1999) reported a greater likelihood for film cracking in systems with elastic-plastic substrates coated with thin layers of high elastic modulus. Stephens et al. (2000) obtained finite element results for

the initial yield behavior of a hard coating/soft substrate system subjected to elliptical normal and friction forces revealing a significant increase of the durability of the layered system with interface exhibiting graded mechanical properties.

The review of the literature indicates that the majority of the analytical and numerical solutions of various indentation problems involving elastic and elastic-plastic layered media are restricted to quasi-static contact conditions. Although important insight into the mechanics of layered media has been derived from these studies, the solutions cannot be applied to dynamic contact problems, such as in nano-/micro-indentation hardness testing. Consequently, the objective of the present study was to develop a comprehensive finite element analysis of dynamic indentation of elastic-plastic multi-layered media. The mesh selection method for unbiased contact analysis due to sound wave reflection from the mesh boundaries is described first, followed by finite element results demonstrating the effects of indentation speed and radius of the rigid cylindrical indenter on the normal force, contact pressure distribution, and subsurface stress-strain field in a multi-layered medium under dynamic indentation loading.

2. Finite Element Mesh for Dynamic Contact Analysis

Sound wave propagation may play an important role in dynamic contact analysis. Two types of bulk waves can propagate in infinite solids: longitudinal waves (also known as dilatational waves because they are characterized by a volume change) and transverse (or shear) waves (Pollard, 1977). In seismology, these two types of waves are often referred to as P (primary) and S (secondary) waves, respectively. In isotropic elastic solids, the propagation speed of a plane dilatational wave, c_p, and a plane shear wave, c_s, are given by

$$c_P = \left(\frac{\lambda + 2G}{\rho} \right)^{1/2} \quad \text{and} \quad c_S = \left(\frac{G}{\rho} \right)^{1/2},$$

where ρ is the material density, and λ and G are the Lamé constants, expressed in terms of the elastic modulus, E, and Poisson's ratio, ν, as

$$\lambda = \frac{E\nu}{(1+\nu)(1-2\nu)} \quad , \quad G = \frac{E}{2(1+\nu)}.$$

It is obvious from the above relations that a plane dilatational wave propagates much faster than a plane shear wave. In addition to these two types of bulk waves, surface waves, such as Rayleigh and Love waves, may be encountered in the case of bounded solids. Since in general the propagation speeds of these surface waves are comparable to those of shear waves (Beltzer, 1988), the attention in this study is restricted to the faster propagating dilatational waves.

2.1 Finite Element Mesh for Homogeneous Medium. In static analysis of infinite half-space media subjected to surface (contact) loads, a reference point is needed in order to obtain displacements due to the singularity of the displacement field under plain strain conditions (Johnson, 1985). This reference point is usually selected to be far away from the contact region. Hence, in plane-strain contact analysis the solution depends on the position of the reference point. However, in dynamic analysis if the displacements in a given region occur within a certain time t_o, then at a fixed point remote from this region there would be no disturbance before the arrival of the propagating waves, i.e., the displacement at any material point ahead of the reflected wave front is zero (Johnson, 1985). Therefore, in dynamic plane-strain contact analysis, if the reference point is selected at a distance sufficiently remote from the contact region such that the waves do not reach this point by the end of the analysis, then the numerical results will be independent of the position of the reference point. Figure 1 shows schematically a propagating dilatational wave in a semi-infinite homogeneous solid. At time t_o, contact is first established at the region around the origin ($x = y = 0$). The dash line represents the dilatational

wave front at time t_1. There is no disturbance in the region ahead of the wave front (region II). Thus, choosing any point in region II as the reference point yields identical simulation results throughout region I for time period $[t_o, t_1]$. In finite element analysis, a finite mesh is used to simulate the semi-infinite half-space. If no waves are generated from the artificial boundaries (i.e., fixed and/or free boundaries), any mesh larger than region I should produce identical results at every point of the mesh within a given time period. Furthermore, the simulation results would be independent of the forces and/or displacements applied on the artificial boundaries to which the waves do not have enough time to propagate. In most applications, the region near the contact interface, where the highest stresses and strains occur, is of interest. In this subsurface region, identical simulation results can be obtained by using a sufficiently large mesh such that the wave(s) reflected from the artificial boundaries do not reach the region of interest before the end of the analysis.

In view of the previous considerations, finite element simulations of dynamic contact were performed with the code ABAQUS using the four meshes shown in Fig. 2. An elastic homogeneous half-space indented by a rigid cylinder at a constant speed of $1 \times 10^{-3}\ c_p$ was modeled in all simulations. Special contact elements were used to model contact between the rigid indenter and the elastic medium. The dimensions of the four meshes, normalized by the radius of the rigid cylinder, R, were chosen to be equal to 6.4×6.4, 12.8×6.4, 6.4×12.8, and 12.8×12.8. Because the left boundary of each mesh is a symmetry axis, all the nodes of this boundary ($x = 0$) were constrained against displacement in the x-direction. The nodes of the bottom boundary were constrained against displacement in the y-direction. All the nodes of the other boundary and the surface were allowed to move freely. The characteristic length of a mesh, l_c, is defined as its smallest dimension. Thus, the characteristic length of the meshes shown in

Figs. 2(a), 2(b), and 2(c) is equal to 6.4R and that of the mesh shown in Fig. 2(d) is equal to 12.8R. In the following discussions, $l_c^{(i)}$ is used to denote the characteristic length of the ith mesh. Obviously, $l_c^{(1)} = l_c^{(2)} = l_c^{(3)} < l_c^{(4)}$. Since in the far field a cylindrical dilatational wave propagates at a speed comparable to that of a plane dilatational wave, the critical time for a dilatational wave propagating from the origin ($x = y = 0$) to the nearest boundary of the meshes shown in Figs. 2(a)-2(c) can be estimated from relation $t_{cr}^{(1)} \approx l_c^{(1)}/c_p$, and the critical time for a wave reflected from the nearest boundary to reach a point in a region close to the origin is approximately equal to $2t_{cr}^{(1)}$.

Figure 3 shows the dimensionless contact load, P/ER, and maximum von Mises stress, $\sigma_M^{\max}/E$, in an elastic half-space as functions of dimensionless time, $t/t_{cr}^{(1)}$, from the onset of indentation, where E is the elastic modulus of the half-space. Since P and $\sigma_M^{\max}$ are mainly related to the stress field in the subsurface region close to the origin, it is clear that for $t \le 2t_{cr}^{(1)}$ the results should be independent of the mesh size. This is confirmed by the results shown in Fig. 3. However, for $t > 2t_{cr}^{(1)}$ the solutions begin to deviate. For the mesh shown in Fig. 2(c) the dilatational wave reflected from the free boundary at $x/R = 6.4$ propagated back first, while for the mesh shown in Fig. 2(b) the dilatational wave reflected from the fixed boundary $y/R = -6.4$ propagated back first. For the mesh shown in Fig. 2(a), the two dilatational waves reflected from the boundaries propagate back to the origin at about the same time. The relatively small discrepancies in the results for the contact force and Mises stress obtained with the meshes shown in Figs. 2(a) and 2(b) and, similarly, those obtained with the meshes shown in Figs. 2(c) and 2(d) indicate that the wave reflected from the bottom boundary exhibits a dominant effect. Both Figs. 3(a) and 3(b) show that discrepancies in the results due to the reflected waves occur at about the same time for the meshes shown in Figs. 2(a) and 2(b) and a little later for the mesh

shown in Fig. 2(c). This implies that the critical time of a mesh (i.e., t_{cr} or ~$2t_{cr}$ if the whole mesh or only a small region of the mesh close to the origin are of interest, respectively) provides a conservative estimation of the maximum time of analysis.

2.2 Finite Element Mesh for Multi-Layered Medium. Similar simulations were performed for an elastic-plastic multi-layered medium using the meshes shown in Fig. 4. The thickness (normalized by the indenter radius) and material properties of the multi-layered medium, given in Table 1 (Kaye et al., 1986; Komvopoulos, 2000), are representative of thin-film disks used in magnetic recording. The material properties and size of the bottom (forth) layer are the same with those of the homogeneous half-space discussed in the previous section. The normalized (by the indenter radius) dimensions of the meshes shown in Figs. 4(a)-4(d) are 6.4 × 7.46, 12.8 × 7.46, 6.4 × 13.86, and 12.8 × 13.86, respectively. Since for the load range analyzed in this study the plastic zone is predicted to be very small compared to the mesh dimensions, the elastic properties of the layered medium control the propagation velocity of the acoustic waves. Figure 5(a) shows that the variation of $\sigma_M^{\max}$ in the surface layer with time and the critical time that the results begin to deviate are similar to those obtained for the elastic homogeneous half-space (Fig. 3(b)). This suggests that wave propagation in the thick (forth) layer plays a predominant role in the stress-strain calculations. Figure 5(b) reveals that the results for the maximum equivalent plastic strain, $\varepsilon_{eq}^{\max}$, in the second soft layer begin to deviate at roughly the same critical time as that of $\sigma_M^{\max}$. This is due to the fact that the locations of $\sigma_M^{\max}$ and $\varepsilon_{eq}^{\max}$ are close to each other and both occur in a subsurface domain adjacent to the contact region.

3. Dynamic Indentation of an Elastic-Plastic Multi-Layered Medium

3.1 Finite Element Modeling and Material Properties of Multi-Layered Medium. Dynamic indentation of a multi-layered medium by a rigid cylinder was analyzed with the finite element code ABAQUS. Contact between the rigid indenter and the multi-layered medium was modeled with rigid surface and second-order contact elements, which were assigned a common reference node that defined the motion of the rigid surface. The rotational and horizontal displacements of the reference node were fully constrained. Indentation was modeled by advancing the rigid surface profile against the deformable mesh using a displacement-control incremental approach. In view of the marginal effect of friction in normal contact (Komvopoulos, 1988), only frictionless indentations were considered in this study. The multi-layered medium was modeled with eight-node, bi-quadratic, plane-strain elements. A 3 × 3 Gaussian integration was used in each element. Because of the symmetry of the geometry and boundary conditions, only one-half of the multi-layered medium (Fig. 6) was modeled, and the nodes on the symmetry axis ($x = 0$) were constrained against displacement in the x-direction. The nodes of the bottom boundary were constrained against displacement in the y-direction. The mesh near the surface was refined, as shown in Fig. 6. The radius of the cylindrical indenter was selected to be equal to $0.2R$, $1.0R$, and $2.0R$, i.e., normalized indenter radius $\widetilde{R}$ = 0.2, 1.0, and 2.0. Hereafter, all the length parameters are normalized by the intermediate indenter radius, R, and are presented in dimensionless form. The smallest elements adjacent to the surface were squares of sides equal to $0.00625R$. The mesh size ($51.2R \times 52.26R$) was selected such that during the time of analysis the reflected waves did not propagate back to the region of interest. The normalized thickness and material properties of the multi-layered medium are listed in Table 1. For simplicity, all layers were assumed to have

Poisson's ratio equal to 0.3. Each layer was modeled as an elastic-perfectly plastic material. The classical von Mises yield criterion was used throughout the simulations.

3.2 Simulation of Dynamic Indentation. Dynamic indentation was modeled by applying incremental displacements to the rigid surface in a controlled fashion that was identical for both loading and unloading. The speed of the indenter was constant during the loading and unloading simulation steps. Simulations were performed for three different indenter speeds of $1 \times 10^{-3}\, c_P^{(4)}$, $2 \times 10^{-3}\, c_P^{(4)}$, and $4 \times 10^{-3}\, c_P^{(4)}$, where $c_P^{(4)}$ is the propagation speed of the plane dilatational waves in the thick substrate (fourth layer). Results are presented in terms of dimensionless indenter speed, $\widetilde{V}$, obtained by dividing the indenter speed by the wave speed $c_P^{(4)}$. The maximum indentation depth was selected to be equal to $0.02R$. While the damping effect was ignored in the simulations of indentation loading and unloading, to obtain solutions for the residual stress-strain field, dashpot elements were added to the mesh after full unloading. The damping coefficients of the dashpot elements were arbitrarily selected to achieve fast equilibrium.

4. Results and Discussion

Finite element solutions for the contact pressure distribution and subsurface stress and strain fields in the multi-layered medium are presented for different values of normalized indentation depth, $\widetilde{\delta}$, speed, $\widetilde{V}$, and indenter radius, $\widetilde{R}$. The propensity for plastic flow and cracking is interpreted in the context of results for the maximum von Mises stress, equivalent plastic strain, and maximum tensile stress in the multi-layered medium during loading and unloading.

4. 1 Contact Force and Contact Pressure Distribution

Figure 7 shows the variation of the contact force, P, with indentation depth, δ, for different values of normalized indentation speed and indenter radius. The contact force is normalized by the critical load, P_Y, corresponding to the inception of yielding in the multi-layered medium due to indentation by a rigid cylinder of intermediate radius ($\widetilde{R}$ = 1.0) penetrating at a relatively high speed ($\widetilde{V}$ = 4 × 10^{-3}). Figure 7(a) shows that the contact force increases monotonically with indentation depth and speed. In dynamic normal contact, a fraction of the external work is dissipated in the form of kinetic energy in the multi-layered medium. Consequently, the higher the indentation speed, the higher the kinetic energy of the system and, hence, the external work supplied to the deforming medium. Moreover, a higher indentation speed produces larger gradients in the displacement field adjacent to the contact region. Therefore, the strains and strain energy intensify with the increase of the indentation speed. Consequently, a higher indentation speed results in a higher contact force for the same surface penetration distance. Figure 7(b) demonstrates that, for a given indentation depth, a lower contact force is obtained with the sharper indenter, evidently due to the correspondingly smaller contact area.

Figure 8 illustrates the dependence of the contact pressure, p, on dimensionless indentation depth, speed, and radius of the rigid indenter. The contact pressure is normalized by the yield strength of the surface layer, σ_{Y1}, and the distance x from the center of contact (x = 0) by the intermediate indenter radius, R. The effect of the various dimensionless parameters on the contact pressure distribution can be explained in terms of the dependence of subsurface plastic deformation on these parameters (discussed in detail in the following section). As shown in Fig. 8(a), increasing the indentation speed intensifies the contact pressure distribution and increases

the contact area, in accord with the contact force results shown in Fig. 7(a). The increase of the maximum contact pressure is a result of the larger strains occurring in a region close to the contact interface, while the increase of the contact area with indentation speed is a consequence of the slower downward movement of the surface of the deforming multi-layered medium compared to the penetrating indenter. Figure 8(b) shows the effect of the indenter radius on the contact pressure distribution for constant indentation depth ($\widetilde{\delta} = 0.02$) and speed ($\widetilde{V} = 4 \times 10^{-3}$). As expected, a higher peak pressure and a smaller contact radius were obtained with the sharper indenter. In the case of the indenter with intermediate radius ($\widetilde{R} = 1.0$), the peak pressure shifts toward the contact edge due to excessive plastic deformation in the second soft layer, conversely to the relatively blunt ($\widetilde{R} = 2.0$) and sharp ($\widetilde{R} = 0.2$) indenters producing a peak pressure at the center of the contact region. This trend is also associated with the effect of the indenter radius on the subsurface stress-strain field. It will be shown later that, due to the much higher yield strength of the surface layer (Table 1), plastic deformation is encountered only in the second (soft) layer. In the case of the large indenter radius, the small value of ratio δ/R leads to less plastic deformation. Regarding the small indenter radius (sharp indenter), the high ratio of the thickness of the surface layer to the contact radius ($t_1/a > 1$) promotes the dominance of elastic deformation in the multi-layered medium and, thus, the peak pressure arises at the center of contact.

4.2 Subsurface Stresses and Evolution of Plasticity

Contours of normalized von Mises equivalent stress, σ_M/σ_{Y1}, in the multi-layered medium obtained from high indentation speed ($\widetilde{V} = 4 \times 10^{-3}$) simulations with an indenter of intermediate radius ($\widetilde{R} = 1.0$) are shown in Fig. 9. In this figure, as well in subsequent stress (strain) contour figures, stress (strain) contours are shown within the first two layers, where the higher stresses

(strains) were encountered in all simulation cases. Stress discontinuities occur at the interface due to the mismatch between the material properties of the first and second layer. For the simulated range of indentation depth ($\widetilde{\delta} \leq 0.02$), the hard surface layer exhibited purely elastic deformation. For relatively small indentation depth ($\widetilde{\delta} = 0.0025$), $\sigma_M^{\max}$ occurs in the surface layer at a depth about half of the contact radius (Fig. 9(a)). However, increasing the indentation depth causes $\sigma_M^{\max}$ to shift toward the interface (Fig. 9(b)). After yielding in the soft layer ($\widetilde{\delta} > 0.005$), $\sigma_M^{\max}$ arises always at the bottom of the hard surface layer near the interface with the plastically deformed soft layer (Figs. 9(b)-9(d)).

Figure 10 illustrates the effects of indentation speed and indenter radius on the evolution of $\sigma_M^{\max}/\sigma_{Y1}$ in the surface layer during the advancement of the rigid indenter into the multi-layered medium. As expected, the Mises stress intensifies with increasing indentation depth, indicating a higher likelihood for yielding in the multi-layered medium, specifically in the soft layer possessing a relatively low yield strength. The trend for $\sigma_M^{\max}$ to increase with indentation speed (Fig. 10(a)) is similar to that observed for the contact force (Fig. 7(a)). The higher values of $\sigma_M^{\max}$ produced with the relatively sharp indenter (Fig. 10(b)) are associated with the high δ/R ratio and the bending effect of the stiffer and harder surface layer.

To further interpret the likelihood of subsurface cracking under both loading and unloading, contours of the normalized first principal (maximum tensile) stress, σ_I/σ_{Y1}, in the multi-layered medium are plotted in Fig. 11 for the case of relatively high indentation speed ($\widetilde{V} = 4 \times 10^{-3}$) and intermediate indenter radius ($\widetilde{R} = 1.0$). Similar to the von Mises stress (Fig. 9), the maximum tensile stress occurs always in the surface layer. In particular, during indentation loading the maximum tensile stress arises at the surface near the contact edge (Figs. 11(a) and

11(b)), while during partial unloading (Fig. 11(c)) and full unloading (Fig. 11(d)) it occurs below the center of the contact region at the interface of the two layers. The results presented in Fig. 11 suggest a greater probability for surface and interfacial cracking during indentation loading and unloading, respectively, depending on the fracture strength of the hard surface layer and the indentation speed and radius of the indenter that affect the magnitude of the maximum tensile stress. This is illustrated in Fig. 12 where the maximum tensile (first principal) stress, $\sigma_I^{\max}$, in the surface layer is plotted as a function of indentation depth for different values of indentation speed and radius of the indenter. The effects of indentation speed and indenter radius on $\sigma_I^{\max}$ become significant at a critical indentation depth $\widetilde{\delta} \geq 0.01$. The variation of $\sigma_I^{\max}$ reveals trends similar to those observed for $\sigma_M^{\max}$ (Fig. 10). As shown in Fig. 12(a), $\sigma_I^{\max}$ in the hard surface layer increases with indentation speed, suggesting a higher propensity for cracking in indentation experiments performed at relatively high loading rates. Cracking may also be enhanced in indentation experiments involving relatively sharp indenters (Fig. 12(b)). Thus, caution should be exercised in nanoindentation hardness tests with thin and hard layers requiring ultra-sharp indenters to avoid the effect of the substrate deformation on the measurement of the layer hardness and elastic modulus.

The evolution of subsurface plasticity in the multi-layered medium may be studied in terms of the equivalent plastic strain, ε_{eq}, contours plotted in Fig. 13 for intermediate indenter radius ($\widetilde{R}$ = 1.0), high indentation speed ($\widetilde{V}$ = 4×10^{-3}), and different indentation depths. Due to the higher yield strength of the surface layer plastic deformation is confined only in the soft layer. At relatively small indentation depth ($\widetilde{\delta}$ = 0.0075), a small plastic zone is produced in the soft layer at the interface with the hard surface layer below the center of contact (Fig. 13(a)). As

the indenter advances deeper into the multi-layered medium ($\widetilde{\delta}$ = 0.0125), the plastic zone grows downward into the soft layer, while $\varepsilon_{eq}^{\max}$ continues to occur along the axis of symmetry (Fig. 13(b)). Deeper penetration of the indenter ($\widetilde{\delta}$ = 0.0175) causes further expansion of the plastic zone and a shift of $\varepsilon_{eq}^{\max}$ toward the interface with the hard surface layer (Fig. 13(c)). At even larger indentation depth ($\widetilde{\delta}$ = 0.02), $\varepsilon_{eq}^{\max}$ commences at the interface of the two layers at a distance about one-third of the corresponding contact radius (Fig. 13(d)). The evolution of $\varepsilon_{eq}^{\max}$ in the present dynamic contact analysis is qualitatively similar to that observed in quasi-static indentation simulations of a homogeneous half-space indented by a rigid sphere (Kral et al., 1993).

To demonstrate the dependence of plasticity in the soft layer on indentation parameters, results for $\varepsilon_{eq}^{\max}$ obtained at different indentations depths during loading and unloading are plotted in Figs. 14 and 15, respectively. Increasing the indentation speed and the sharpness of the indenter contributes to the premature yielding of the soft layer. For the range of parameters examined in this study, the critical indentation depth at the inception of yielding is predicted to be between 0.004 and 0.011, depending on the speed and radius of the indenter (Fig. 14). The dependence of $\varepsilon_{eq}^{\max}$ on indentation parameters (i.e., $\widetilde{\delta}$, $\widetilde{V}$, and $\widetilde{R}$) exhibits trends similar to those observed for $\sigma_M^{\max}$ (Fig. 10) and $\sigma_I^{\max}$ (Fig. 12). Figure 15 shows that reyielding during unloading depends on the speed and radius of the indenter. Dynamic unloading from a maximum depth $\widetilde{\delta}$ = 0.02 is fully elastic for all simulation cases except for that involving the relatively sharper indenter ($\widetilde{R}$ = 0.2) and higher load/unload speed ($\widetilde{V}$ = 4×10^{-3}). For this case, additional plastic deformation begins to accumulate in the soft layer as soon as the indenter is retracted to a

depth $\widetilde{\delta} \simeq 0.01$. The region where reyielding occurs in the soft layer is below the center of contact, close to the interface with the hard surface layer.

4.3 Residual Stress-Strain Field

As mentioned previously, damping was not included in the dynamic simulations of indentation loading and unloading. Consequently, after dynamic unloading, the multi-layered medium continued to oscillate without ever reaching equilibrium due to the reflection of waves from the boundaries. Therefore, as mentioned in section 3.2, to enable the analysis of the residual stress-strain field due to dynamic indentation, dashpot elements were added to the finite element mesh after full unloading. The damping coefficients of these elements were selected such that the vibration of the unloaded medium decreased in a short time. Since additional plastic deformation due to the vibration of the multi-layered medium does not occur, the residual stress-strain field can be obtained as soon as equilibrium is reached. Contours of residual σ_M and ε_{eq} are shown in Figs. 16 and 17, respectively, for different values of normalized indenter radius and indentation speed. The results obtained for the same indenter radius ($\widetilde{R} = 1.0$) reveal that increasing the indentation speed causes intensification of the residual stress field in the hard surface layer (especially at the interface with the soft layer) (Figs. 16(a)-16(c)) and promotes the development of higher residual plastic strains and larger plastic zone in the soft layer (Figs. 17(a)-17(c)) below the center of contact. A comparison of Figs. 16(c) and 17(c) with Figs. 16(d) and 17(d), respectively, shows that the residual stresses and plastic strains in the hard and soft layers, respectively, increase significantly with the sharpness of the indenter, while the size of the plastic zone in the soft layer decreases slightly. The development of $\sigma_M^{\max}$ at the bottom of the hard layer below the center of contact is attributed to bending of the elastically deformed hard layer as the

soft layer flows plastically. The resulting large stress gradients across the interface are associated with the occurrence of $\varepsilon_{eq}^{\max}$ in the soft layer adjacent to the region of $\sigma_M^{\max}$ at the bottom of the hard surface layer.

Summarizing, the results of this study demonstrate the effect of indentation depth, speed, and sharpness of the indenter on the elastic-plastic deformation and likelihood of cracking in multi-layered media. The dimensionless form of the results allows interpretation of a large number of cases matching the dimensionless indentation parameters. The findings of this work provide explanation to phenomenological observations of mechanical failure in layered media due to excessive plastic flow and cracking in indentation experiments. The present finite element model can be easily extended to account for strain hardening and strain rate sensitivity effects under dynamic contact loading.

5. Conclusions

A plane-strain dynamic contact analysis for an elastic-plastic multi-layered medium indented by a rigid cylinder of varying radius was performed using the finite element method. Solutions for the contact force, contact pressure, and subsurface stresses and strains were obtained in terms of penetration depth, indenter radius, and indentation speed for both loading and unloading. Based on the presented results and discussion, the following main conclusions can be drawn from this study.

(1) For dynamic contact analysis of semi-infinite half-space media with the finite element technique, a sufficiently large mesh is required in order for the faster propagating dilatational waves reflected from the mesh boundaries not to reach the region of analysis

within the time of analysis. In this region, the simulation results are independent of the mesh dimensions, and specifying a reference node for the displacements is not necessary.

(2) Wave propagation in the multi-layered medium examined in this study was dominated by the material properties of the thick substrate (forth layer) of the half-space medium.

(3) The contact load, contact pressure, and subsurface stresses and plastic strains (both loading and residual) increase with indentation depth and speed. Higher indentation speed leads to premature yielding and plastic zone formation in the second (soft) layer and higher tensile stresses in the elastically deformed (for the simulated material properties and indentation parameters of this study) surface (hard) layer.

(4) A sharper indenter yields a smaller critical indentation depth at the inception of yielding, higher peak contact pressure, lower contact load, and intensified subsurface stress-strain field. Due to the high yield strength of the surface layer the peak value of the maximum von Mises equivalent stress occurs always in this layer, whereas the peak equivalent plastic strain arises always in the soft layer.

(5) Results for the peak values and locations of the maximum von Mises equivalent stress, first principal stress, and maximum equivalent plastic strain as well as the evolution of the plastic zone during indentation loading and unloading obtained in terms of dimensionless indentation parameters. The dimensionless solutions provide insight into the propensity for plastic flow and cracking in dynamically indented multi-layered media.

Acknowledgments

This research was funded by the National Science Foundation through a grant from Carnegie Mellon University (Award No. 1002071-105936) and the Computer Mechanics Laboratory at the University of California at Berkeley.

References

Beltzer, A. I., *Acoustics of Solids* (Springer-Verlag, Berlin Heidelberg, 1988).

Brock, L. M., Georgiadis, H. G., 1994, "Dynamic Frictional Indentation of an Elastic Half-Plane by a Rigid Punch," Journal of Elasticity, **35**, pp 223-249.

Burmister, D. M., 1945, "The General Theory of Stresses and Displacements in Layered Systems," Journal of Applied Physics, **16**, pp. 89-94, 126-127, and 296-302.

Dhaliwal, R. S., and Rau, I. S., 1970, "Axisymmetric Boussinesq Problem for a Thick Elastic Layer under a Punch of Arbitrary Profile," International Journal of Engineering Science, **8**, pp. 843-856.

Faulkner, A., Tang, K. C., Sen, S., and Arnell, R. D., 1998, "Finite Element Solutions Comparing the Normal Contact of an Elastic-Plastic Layered Medium under Loading by (a) a Rigid and (b) a Deformable Indenter," Journal of Strain Analysis, **33**, pp. 411-418.

Gan, L., and Ben-Nissan, B., 1997, "The Effects of Mechanical Properties of Thin Films on Nano-Indentation Data: Finite Element Analysis," Computational Materials Science, **8**, pp. 273-281.

Gupta, P. K., and Walowit, J. A., 1974, "Contact Stresses between an Elastic Cylinder and a Layered Elastic Solid," ASME Journal of Tribology, **96**, pp. 250-257.

Johnson, K. L, 1985, *Contact Mechanics* (Cambridge University Press, Cambridge, UK).

Kaye, G. W. C., 1986, *Tables of Physical and Chemical Constants and Some Mathematical Functions* (Longman, London, UK).

Kennedy, F. E., and Ling, F. F., 1974, "Elasto-Plastic Indentation of a Layered Medium," ASME Journal of Engineering Materials and Technology, **96**, pp. 97-103.

King, R. B., and O'Sullivan, T. C., 1987, "Sliding Contact Stress in a Two-Dimensional Layered Elastic Half-Space," International Journal of Solids and Structures, **23**, pp. 581-597.

Komvopoulos, K., 1988, "Finite Element Analysis of a Layered Elastic Solid in Normal Contact With a Rigid Surface," ASME Journal of Tribology, **110**, pp. 477-485.

Komvopoulos, K., 1989, "Elastic-Plastic Finite Element Analysis of Indented Layered Media," ASME Journal of Tribology, **111**, pp. 430-439.

Komvopoulos, K., 2000, "Head-Disk Interface Contact Mechanics for Ultrahigh Density Magnetic Recording," Wear, **238**, pp. 1-11.

Kral, E. R., Komvopoulos, K., and Bogy, D. B., 1993, "Elastic-Plastic Finite Element Analysis of Repeated Indentation of a Half-Space by a Rigid Sphere," ASME Journal of Applied Mechanics, **60**, pp. 829-841.

Kral, E. R., Komvopoulos, K., and Bogy, D. B., 1995a, "Finite Element Analysis of Repeated Indentation of an Elastic-Plastic Layered Medium by a Rigid Sphere, Part I: Surface Results," ASME Journal of Applied Mechanics, **62**, pp. 20-28.

Kral, E. R., Komvopoulos, K., and Bogy, D. B., 1995b, "Finite Element Analysis of Repeated Indentation of an Elastic-Plastic Layered Medium by a Rigid Sphere, Part II: Subsurface Results," ASME Journal of Applied Mechanics, **62**, pp. 29-42.

Montmitonnet, P., Edlinger, M. L., and Felder, E., 1993, "Finite Element Analysis of Elastoplastic Indentation: Part II-Application to Hard Coatings," ASME Journal of Tribology, **115**, pp. 15-19.

Pollard, H. F., *Sound Waves in Solids* (Pion, London, UK, 1977).

Sen, S., Aksakal, B., and Ozel, A., 1998, "A Finite-Element Analysis of the Indentation of an Elastic-Work Hardening Layered Half-space by an Elastic Sphere," International Journal of Mechanical Sciences, **40**, pp. 1281-1293.

Souza, R. M., Mustoe, G. G. W., and Moore, J. J., 1999, "Finite-Element Modeling of the Stresses and Fracture during the Indentation of Hard Elastic Films on Elastic-Plastic Aluminum Substrates," Thin Solid Films, **335-336**, pp. 303-310.

Stephens, L. S., Liu, Y., and Meletis, E. I., 2000, "Finite Element Analysis of the Initial Yielding Behavior of a Hard Coating/Substrate System with Functionally Graded Interface under Indentation and Friction," ASME Journal of Tribology, **122**, pp. 381-387.

Table 1. Thickness and material properties of the layered medium*

Medium	Normalized thickness (t/R)	Elastic modulus (GPa)	Yield strength (GPa)	Density (kg/m^3)
Layer 1	0.05	168	13.0	2266
Layer 2	0.156	130	2.67	8800
Layer 3	0.08	140	2.58	7000
Layer 4	6.4, 12.8, 51.2	160	2.67	8000

* Sources: Kaye et al. (1986); Komvopoulos (2000); $\nu = 0.3$ (for all layers).

List of Figures

radius ($\widetilde{R}$ = 1.0) and (b) varying indenter radius and constant indentation speed ($\widetilde{V}$ = 4×10^{-3}).

Fig. 8 Contact pressure distribution on elastic-plastic multi-layered medium indented by a rigid cylinder for (a) varying indentation depth and speed and constant indenter radius ($\widetilde{R}$ = 1.0) and (b) varying indenter radius and constant indentation depth ($\widetilde{\delta}$ = 0.02) and speed ($\widetilde{V}$ = 4×10^{-3}).

Fig. 9 Contours of von Mises equivalent stress in elastic-plastic multi-layered medium indented by a rigid cylinder of intermediate radius ($\widetilde{R}$ = 1.0) at constant indentation speed ($\widetilde{V}$ = 4×10^{-3}) for indentation depth (a) $\widetilde{\delta}$ = 0.0025, (b) $\widetilde{\delta}$ = 0.0075, (c) $\widetilde{\delta}$ = 0.015, and (d) $\widetilde{\delta}$ = 0.02.

Fig. 10 Maximum von Mises equivalent stress in the surface (hard) layer of an elastic-plastic multi-layered medium indented by a rigid cylinder versus indentation depth for (a) varying indentation speed and constant indenter radius ($\widetilde{R}$ = 1.0) and (b) varying indenter radius and constant indentation speed ($\widetilde{V}$ = 4×10^{-3}).

Fig. 11 Contours of first principal stress in elastic-plastic multi-layered medium indented by a rigid cylinder of intermediate radius ($\widetilde{R}$ = 1.0) at constant indentation speed ($\widetilde{V}$ = 4×10^{-3}) for indentation depth (a) $\widetilde{\delta}$ = 0.01 (loading), (b) $\widetilde{\delta}$ = 0.02 (loading), (c) $\widetilde{\delta}$ = 0.01 (partial unloading), and (d) $\widetilde{\delta}$ = 0 (full unloading).

Fig. 12 Maximum tensile (first principal) stress in the surface (hard) layer of an elastic-plastic multi-layered medium indented by a rigid cylinder versus indentation depth for (a) varying indentation speed and constant indenter radius ($\widetilde{R}$ = 1.0) and (b) varying indenter radius and constant indentation speed ($\widetilde{V}$ = 4×10^{-3}).

Fig. 13 Contours of equivalent plastic strain in elastic-plastic multi-layered medium indented by a rigid cylinder of intermediate radius ($\widetilde{R}$ = 1.0) at constant indentation speed ($\widetilde{V}$ = 4×10^{-3}) for indentation depth (a) $\widetilde{\delta}$ = 0.0075, (b) $\widetilde{\delta}$ = 0.0125, (c) $\widetilde{\delta}$ = 0.0175, and (d) $\widetilde{\delta}$ = 0.02.

Fig. 14 Maximum equivalent plastic strain in the second (soft) layer of an elastic-plastic multi-layered medium indented by a rigid cylinder versus indentation depth for (a) varying indentation speed and constant indenter radius ($\widetilde{R}$ = 1.0) and (b) varying indenter radius and constant indentation speed ($\widetilde{V}$ = 4×10^{-3}).

Fig. 15 Maximum equivalent plastic strain in the second (soft) layer of an elastic-plastic multi-layered medium indented by a rigid cylinder during unloading versus indentation depth for varying indentation speed and indenter radius.

Fig. 16 Contours of residual von Mises equivalent stress in elastic-plastic multi-layered medium indented by a rigid cylinder after full unloading for different values of indentation speed and indenter radius: (a) $\widetilde{V}$ = 1×10^{-3}, $\widetilde{R}$ = 1.0, (b) $\widetilde{V}$ = 2×10^{-3}, $\widetilde{R}$ = 1.0, (c) $\widetilde{V}$ = 4×10^{-3}, $\widetilde{R}$ = 1.0, and (d) $\widetilde{V}$ = 4×10^{-3}, $\widetilde{R}$ = 0.2.

Fig. 17 Contours of residual equivalent plastic strain in elastic-plastic multi-layered medium indented by a rigid cylinder after full unloading for different values of indentation speed and indenter radius: (a) $\widetilde{V}$ = 1×10^{-3}, $\widetilde{R}$ = 1.0, (b) $\widetilde{V}$ = 2×10^{-3}, $\widetilde{R}$ = 1.0, (c) $\widetilde{V}$ = 4×10^{-3}, $\widetilde{R}$ = 1.0, and (d) $\widetilde{V}$ = 4×10^{-3}, $\widetilde{R}$ = 0.2.

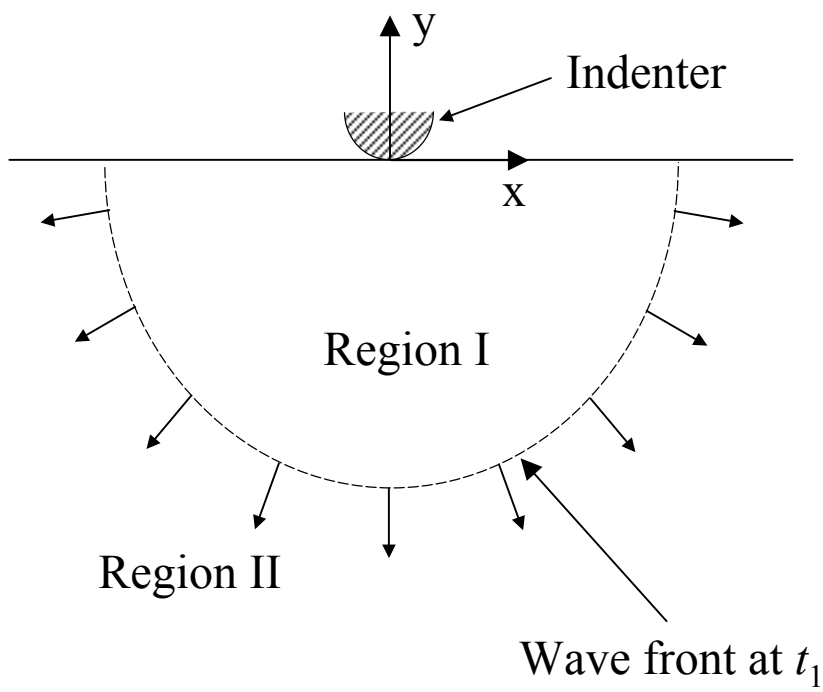

Fig. 1

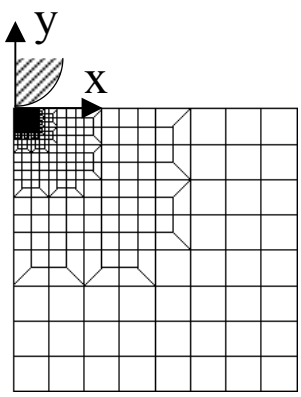

(a)

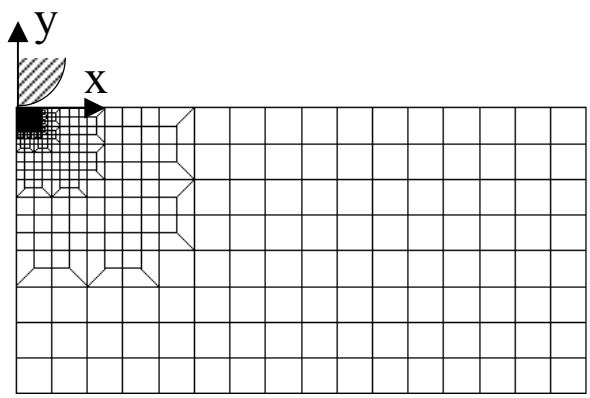

(b)

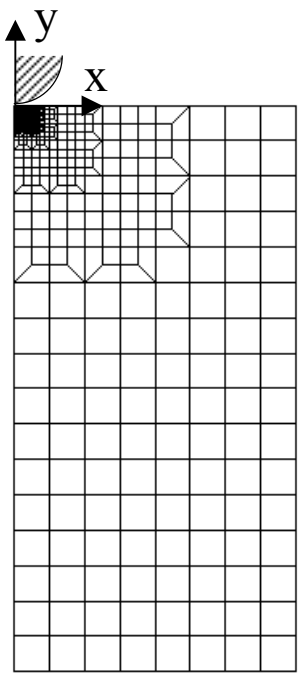

(c)

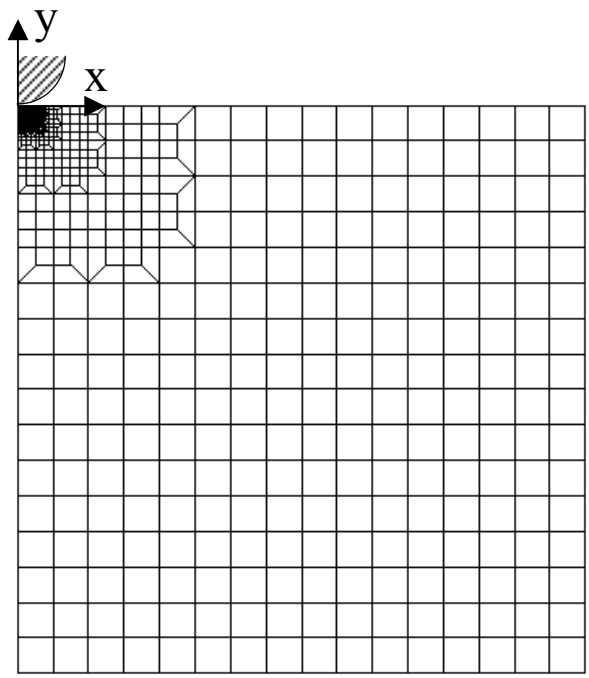

(d)

Fig. 2

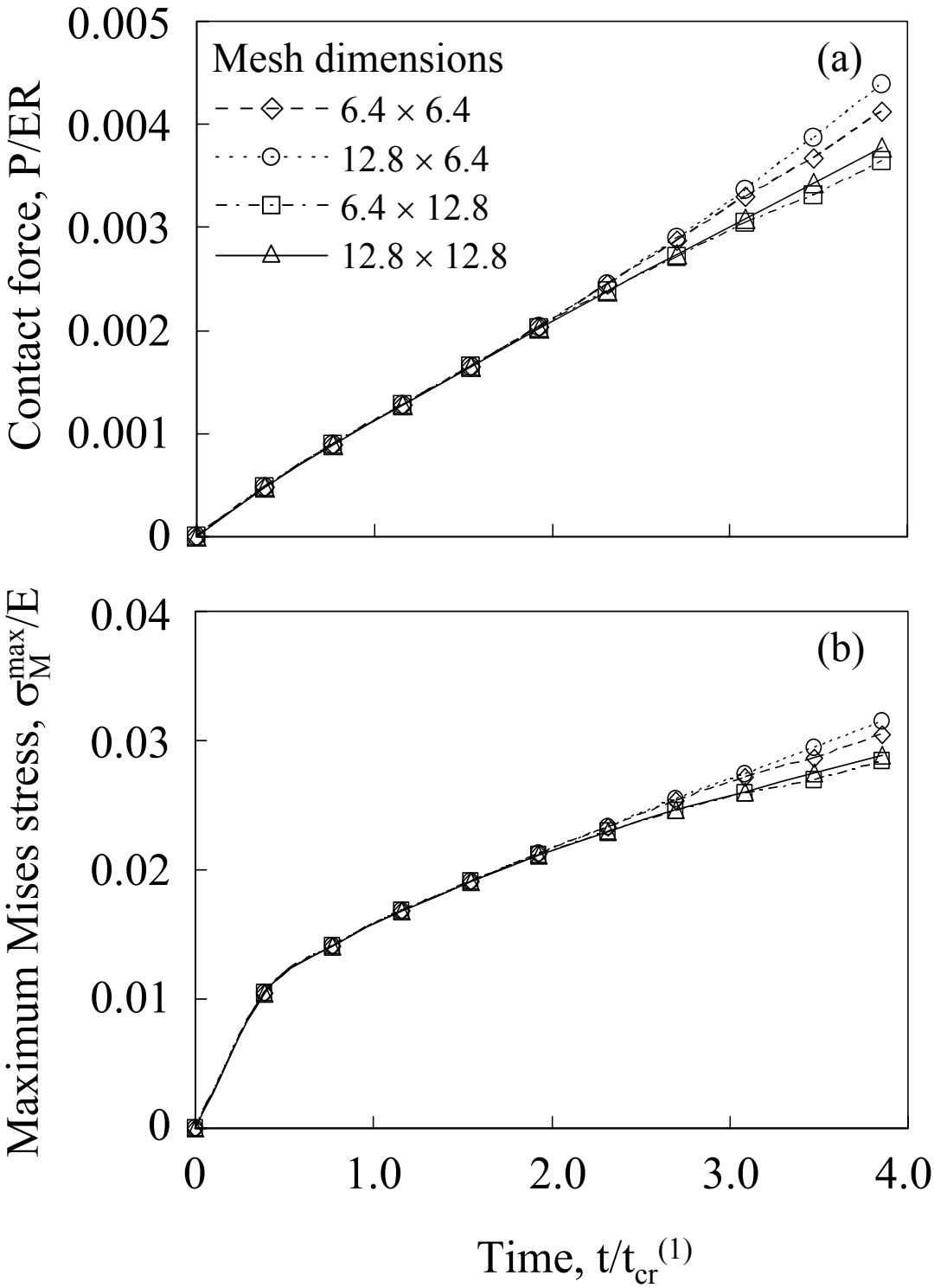
Mesh dimensions
6.4 × 6.4
12.8 × 6.4
6.4 × 12.8
12.8 × 12.8
(a)
(b)
Contact force, P/ER
Maximum Mises stress, σ_M^{max}/E
Time, $t/t_{cr}^{(1)}$
0.005
0.004
0.003
0.002
0.001
0
0.04
0.03
0.02
0.01
0
1.0
2.0
3.0
4.0

Fig. 3

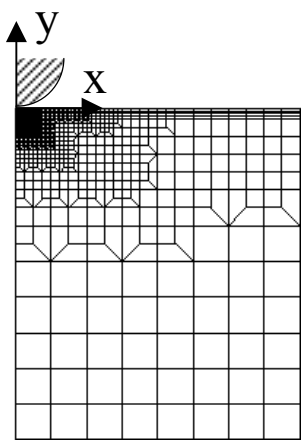

(a)

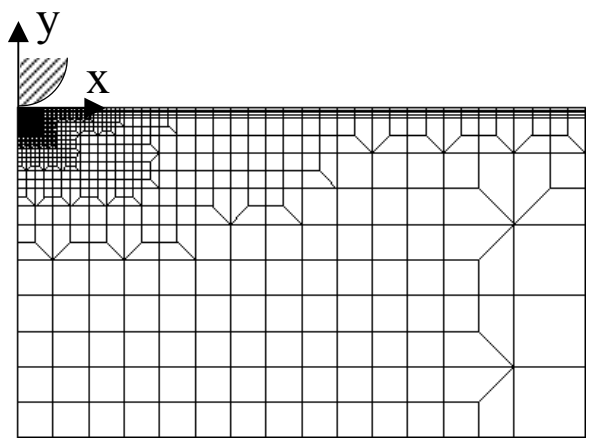

(b)

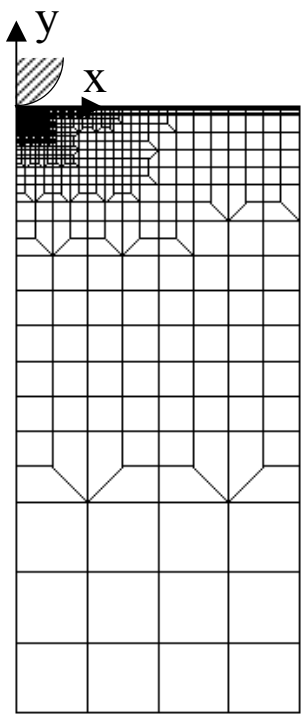

(c)

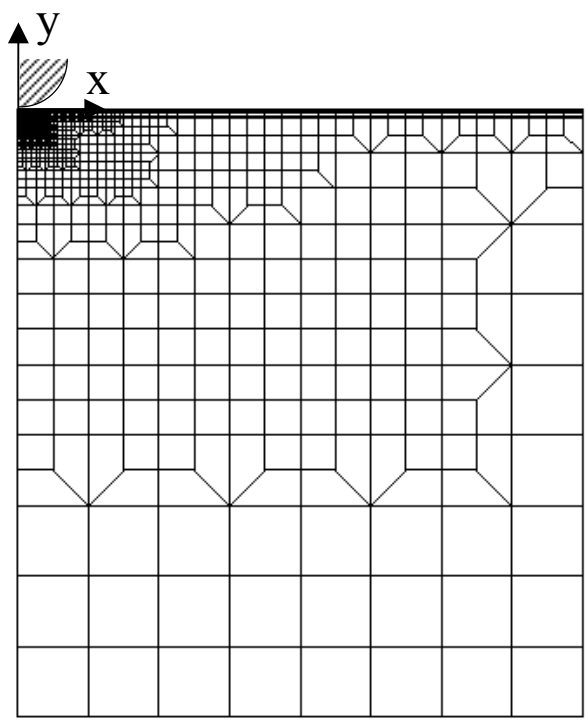

(d)

Fig. 4

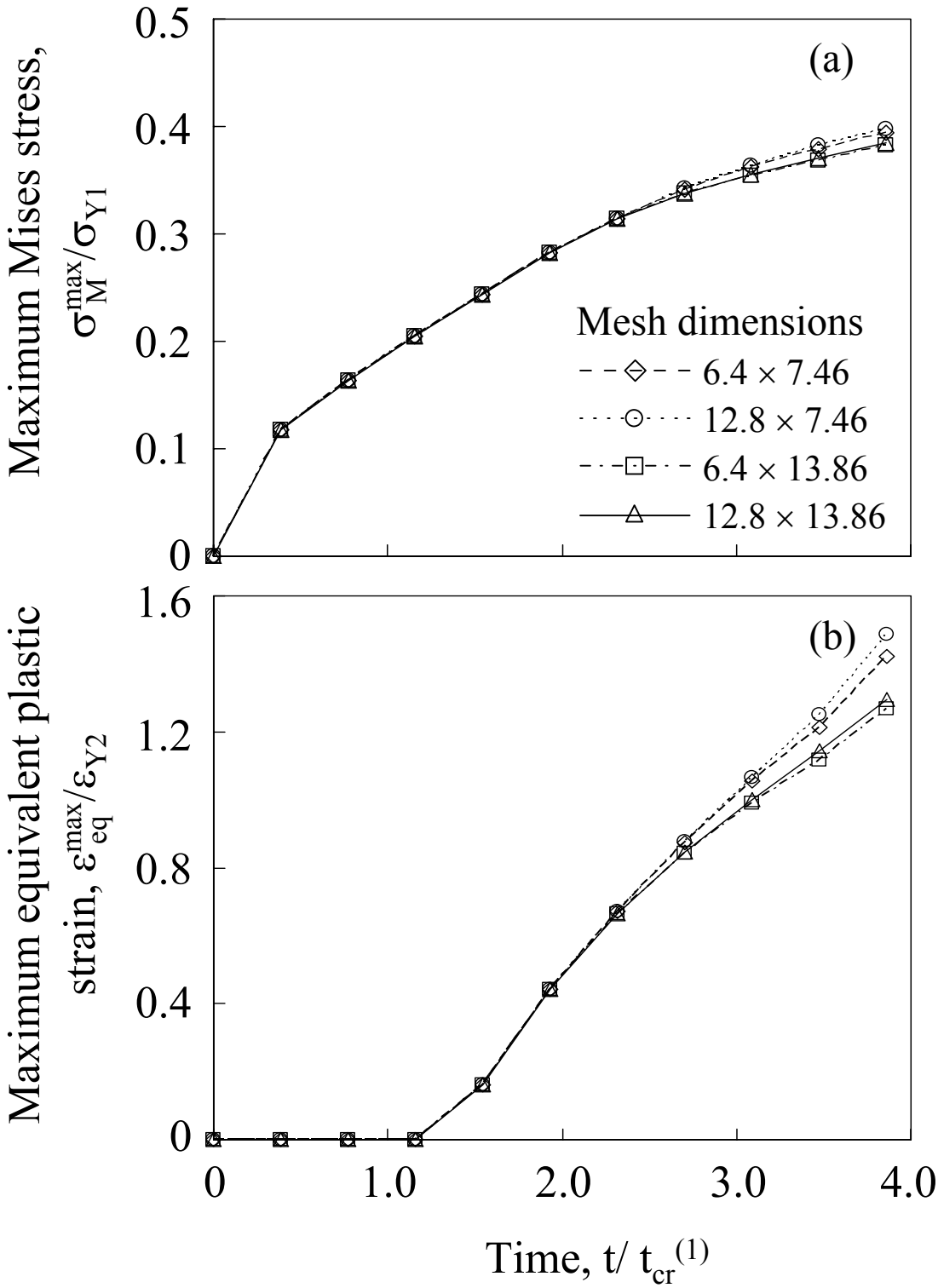
(a)
Maximum Mises stress, $\sigma_M^{max}/\sigma_{Y1}$
0.5
0.4
0.3
0.2
0.1
0
Mesh dimensions
6.4 × 7.46
12.8 × 7.46
6.4 × 13.86
12.8 × 13.86
(b)
Maximum equivalent plastic strain, $\varepsilon_{eq}^{max}/\varepsilon_{Y2}$
1.6
1.2
0.8
0.4
0
0
1.0
2.0
3.0
4.0
Time, $t/\ t_{cr}^{(1)}$

Fig. 5

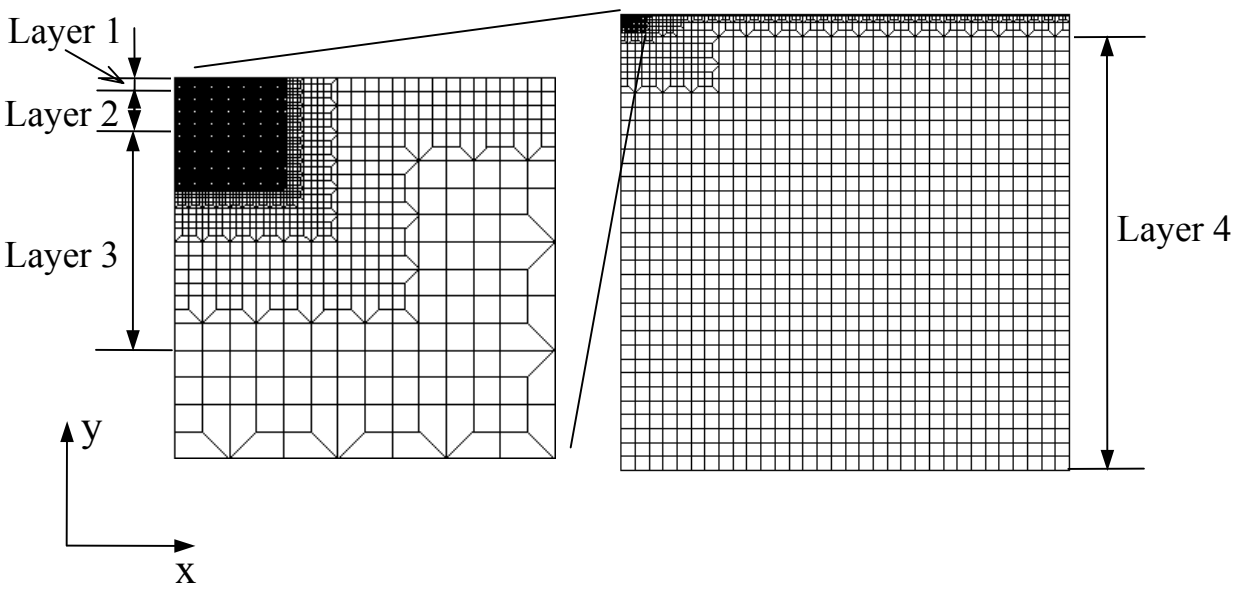

Fig. 6

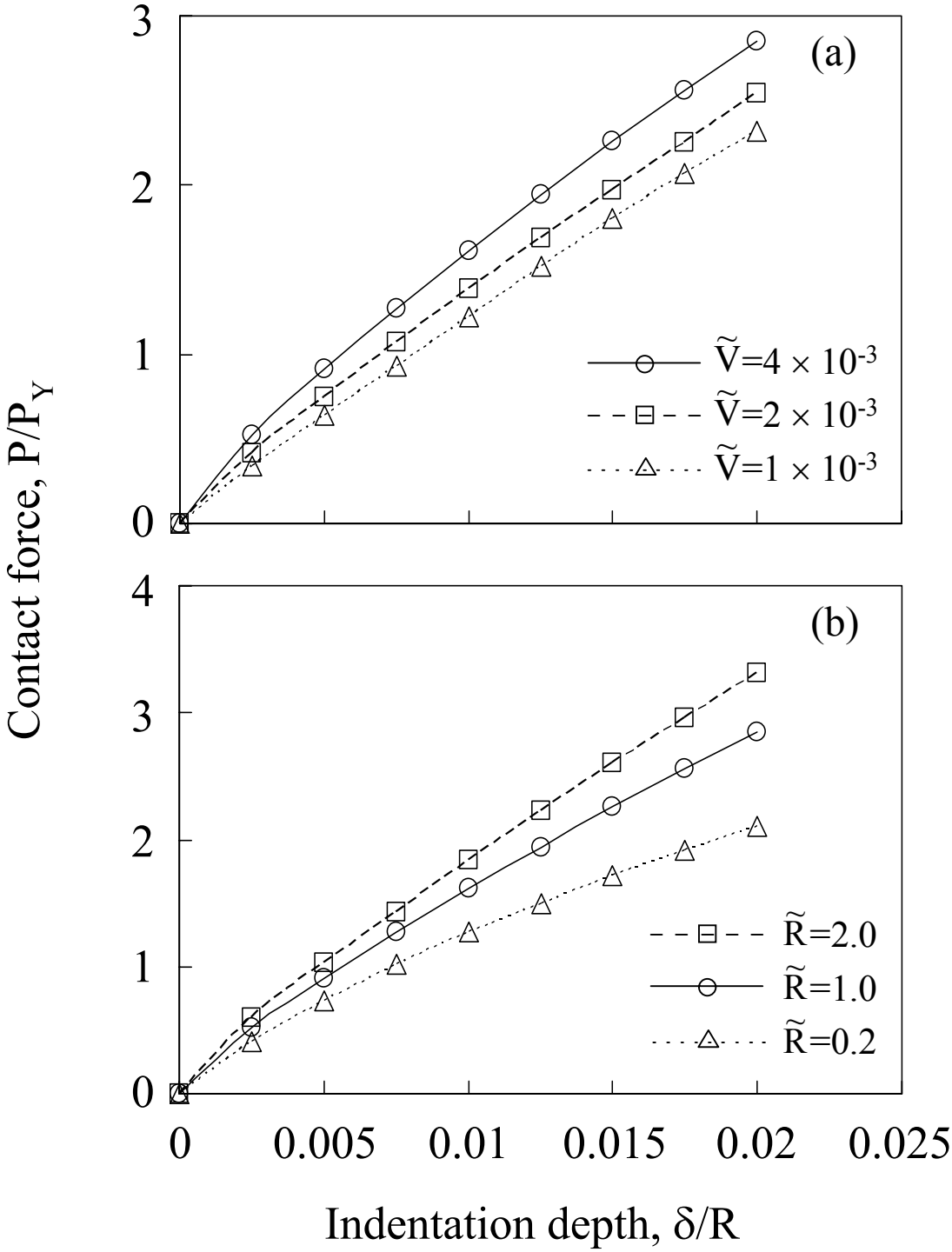
(a)
$\tilde{V}=4\times10^{-3}$
$\tilde{V}=2\times10^{-3}$
$\tilde{V}=1\times10^{-3}$
(b)
$\tilde{R}=2.0$
$\tilde{R}=1.0$
$\tilde{R}=0.2$
Contact force, P/P_Y
Indentation depth, δ/R
0
1
2
3
4
0.005
0.01
0.015
0.02
0.025

Fig. 7

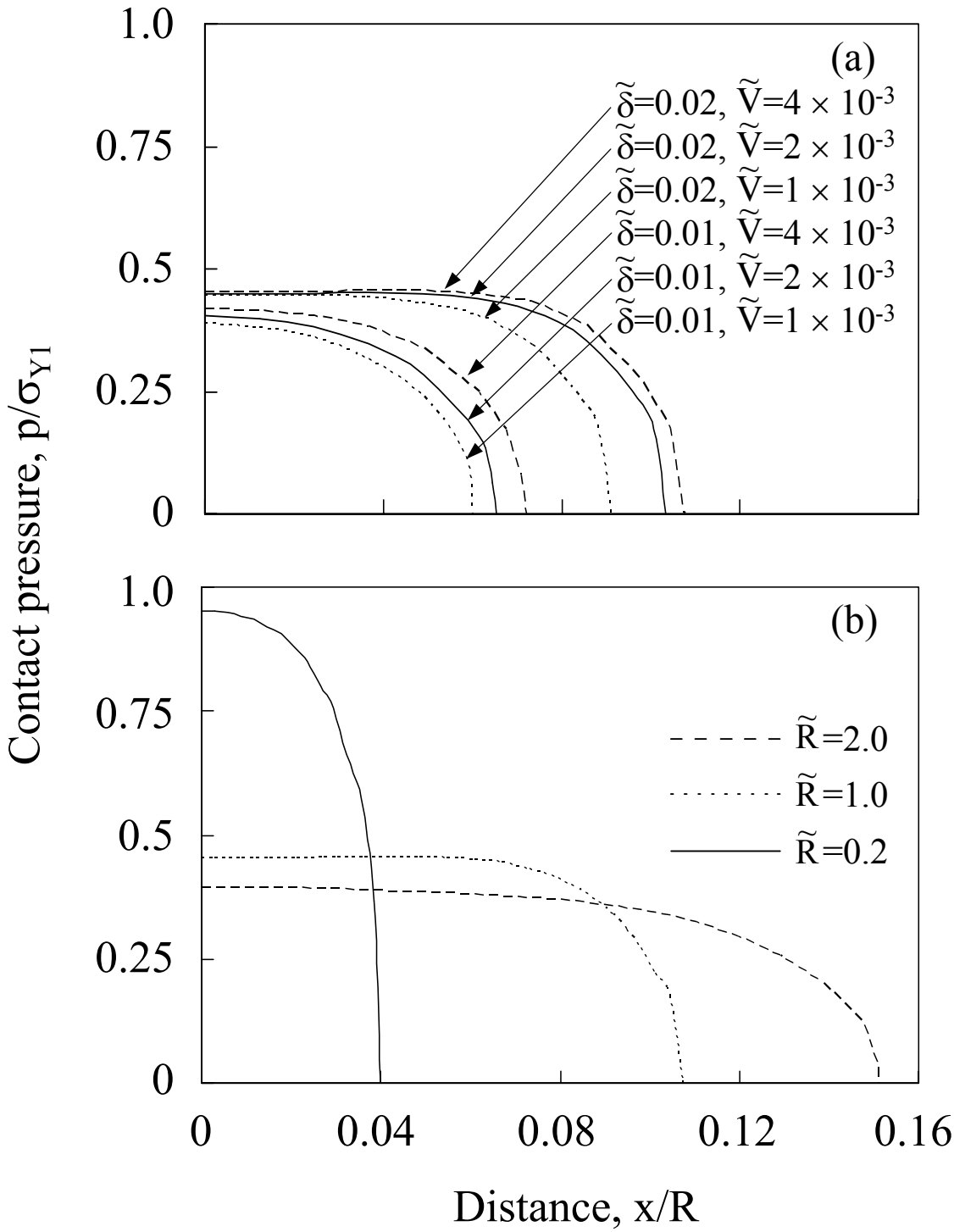
(a)
δ̃=0.02, Ṽ=4 × 10-3
δ̃=0.02, Ṽ=2 × 10-3
δ̃=0.02, Ṽ=1 × 10-3
δ̃=0.01, Ṽ=4 × 10-3
δ̃=0.01, Ṽ=2 × 10-3
δ̃=0.01, Ṽ=1 × 10-3
(b)
R̃=2.0
R̃=1.0
R̃=0.2
Contact pressure, p/σY1
Distance, x/R
1.0
0.75
0.5
0.25
0
0
0.04
0.08
0.12
0.16

Fig. 8

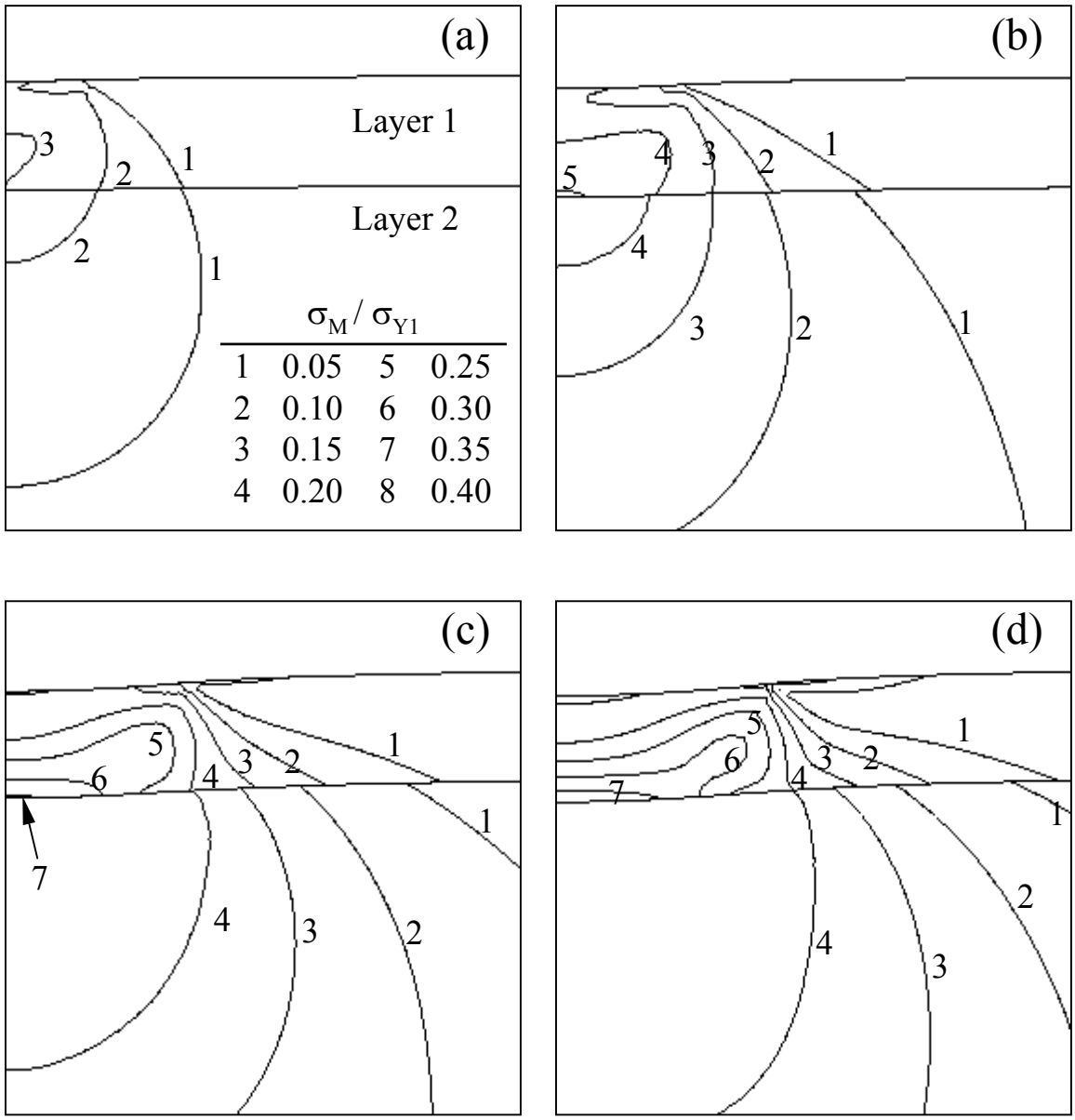
(a)
Layer 1
Layer 2
3
2
1
2
1
σ_M / σ_{Y1}
1 0.05 5 0.25
2 0.10 6 0.30
3 0.15 7 0.35
4 0.20 8 0.40
(b)
5
4
3
2
1
4
3
2
1
(c)
6
5
4
3
2
1
1
7
4
3
2
(d)
6
5
4
3
2
1
7
1
4
3
2

Fig. 9

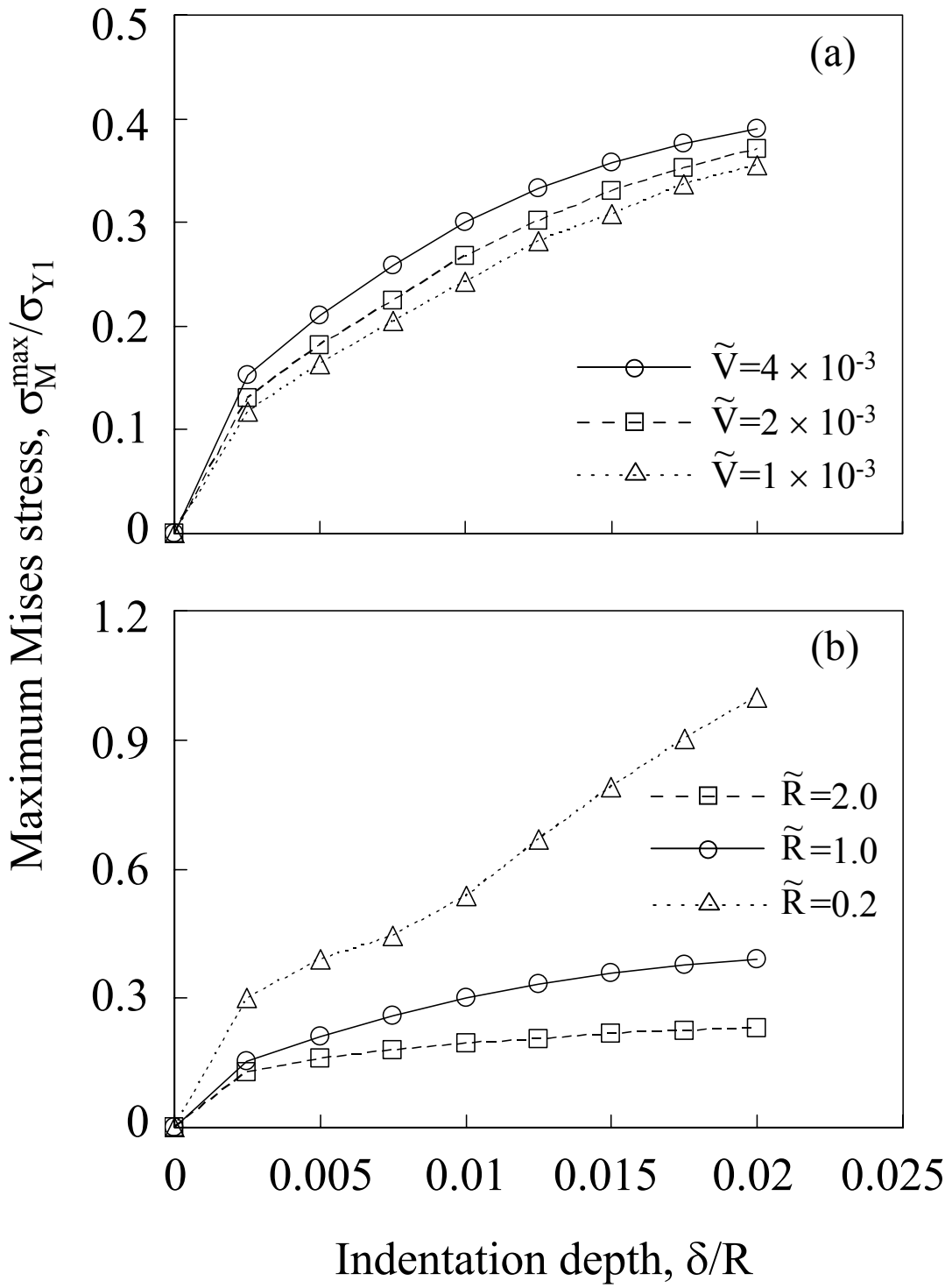
(a)
(b)
Maximum Mises stress, $\sigma_M^{max}/\sigma_{Y1}$
Indentation depth, δ/R
$\tilde{V}$=4 × 10^{-3}
$\tilde{V}$=2 × 10^{-3}
$\tilde{V}$=1 × 10^{-3}
$\tilde{R}$=2.0
$\tilde{R}$=1.0
$\tilde{R}$=0.2
0
0.1
0.2
0.3
0.4
0.5
0.6
0.9
1.2
0.005
0.01
0.015
0.02
0.025

Fig. 10

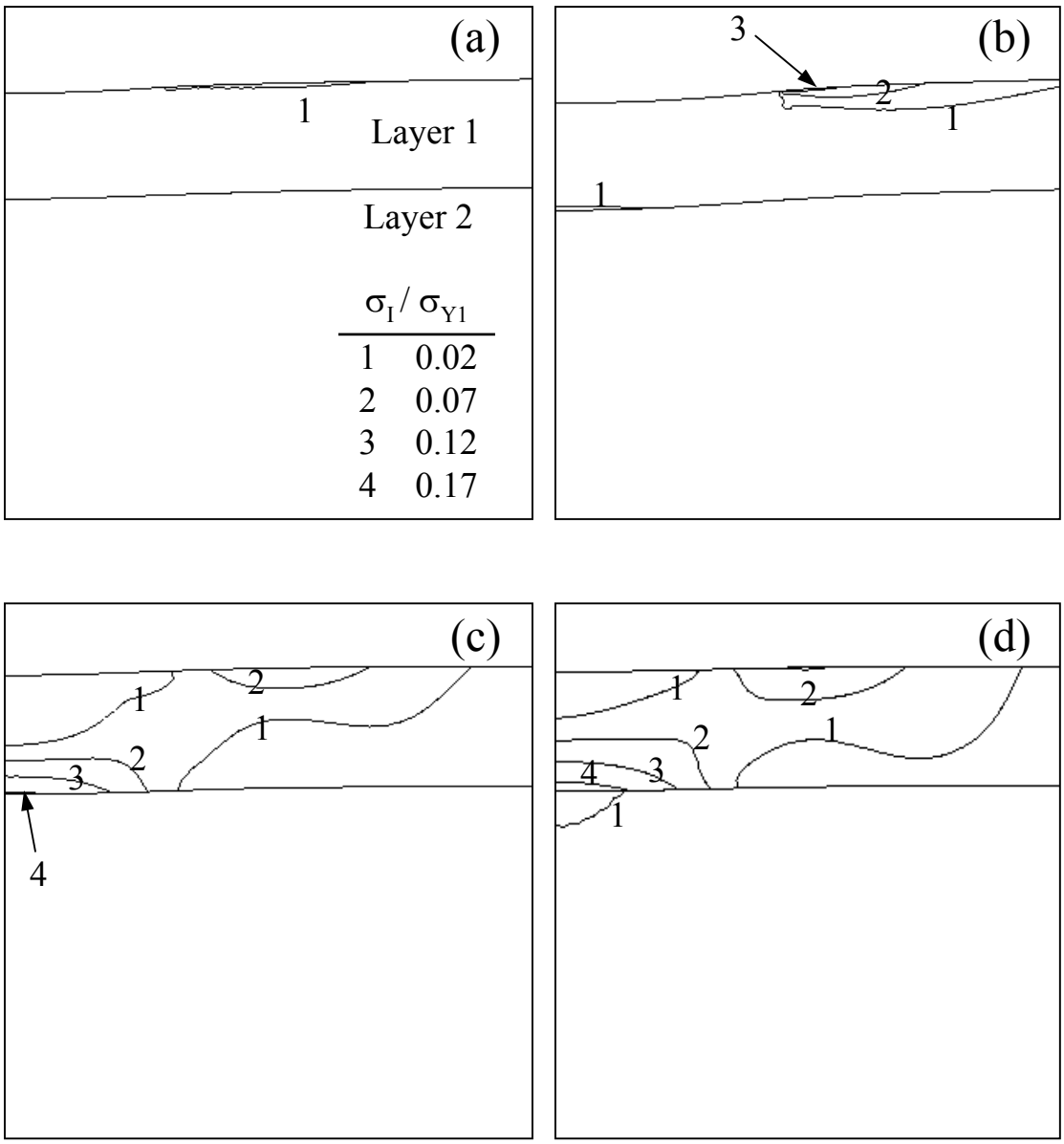
(a)
1
Layer 1
Layer 2
σI / σY1
1 0.02
2 0.07
3 0.12
4 0.17
(b)
3
2
1
1
(c)
1
2
1
2
3
4
(d)
1
2
2
1
4
3
1

Fig. 11

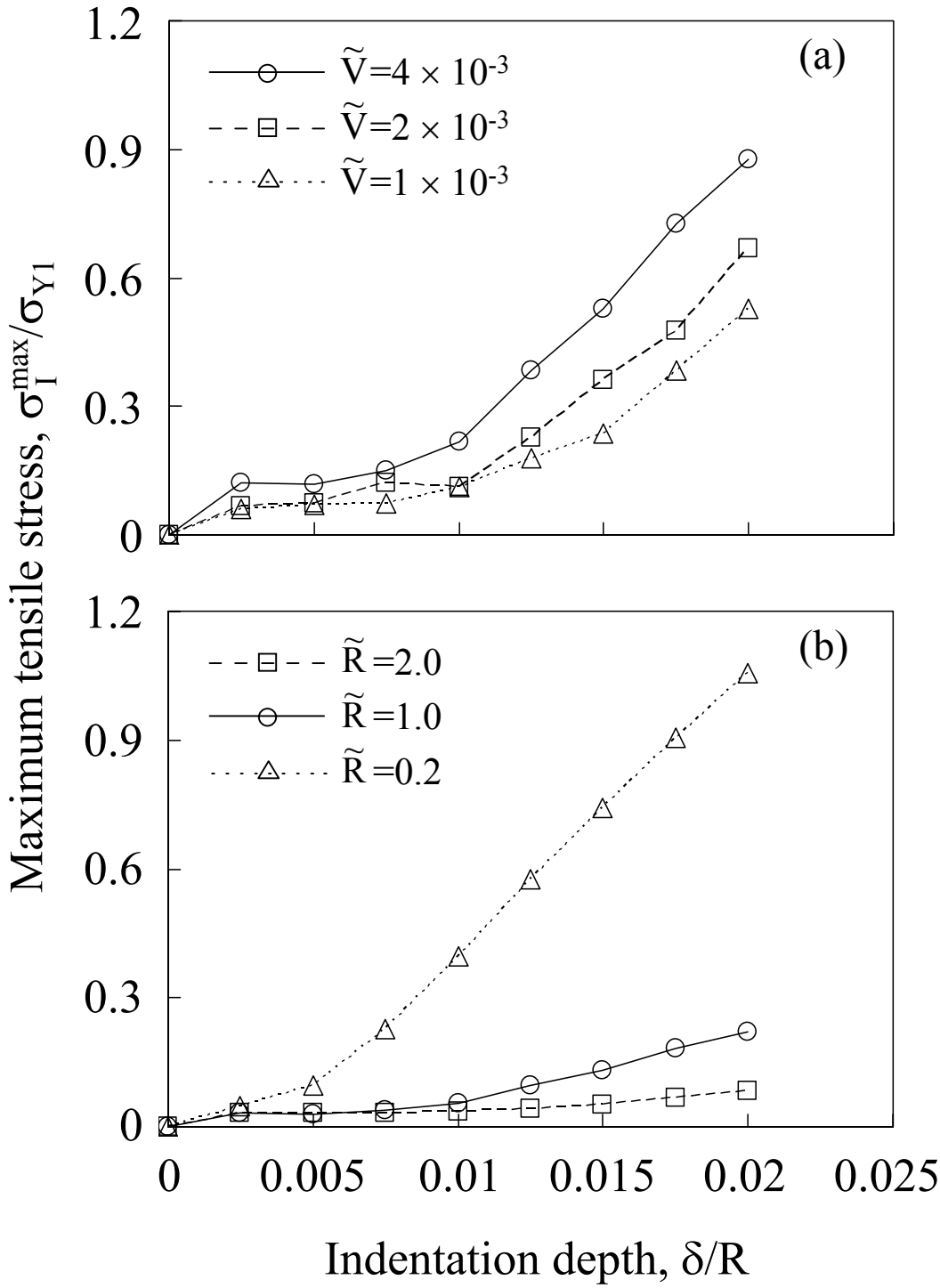
(a)
$\tilde{V}$=4 × 10-3
$\tilde{V}$=2 × 10-3
$\tilde{V}$=1 × 10-3
(b)
$\tilde{R}$=2.0
$\tilde{R}$=1.0
$\tilde{R}$=0.2
Maximum tensile stress, $\sigma_I^{max}/\sigma_{Y1}$
Indentation depth, δ/R
0
0.3
0.6
0.9
1.2
0.005
0.01
0.015
0.02
0.025

Fig. 12

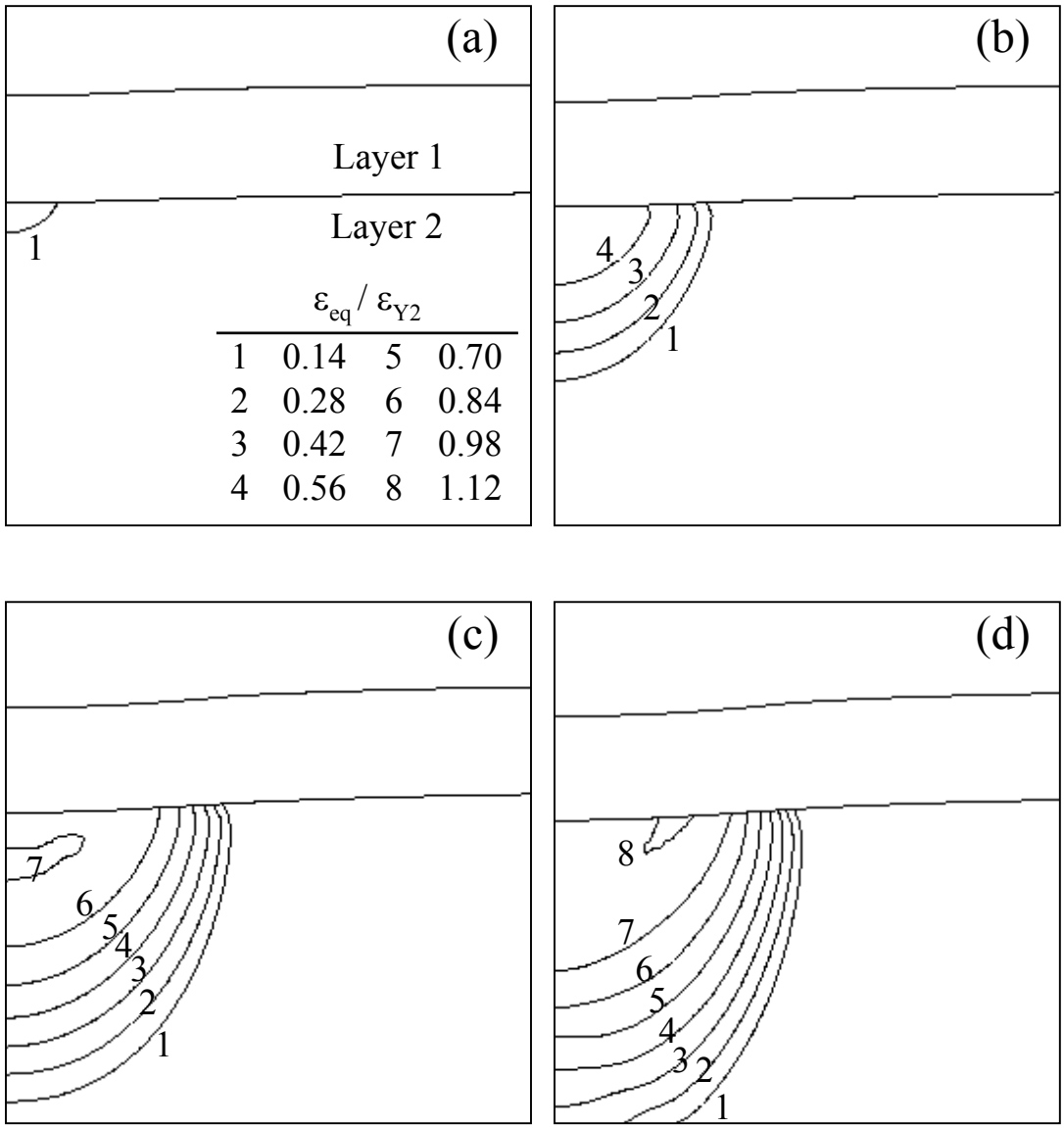
(a)
Layer 1
Layer 2
1
$\varepsilon_{eq} / \varepsilon_{Y2}$
1 0.14 5 0.70
2 0.28 6 0.84
3 0.42 7 0.98
4 0.56 8 1.12
(b)
4
3
2
1
(c)
7
6
5
4
3
2
1
(d)
8
7
6
5
4
3
2
1

Fig. 13

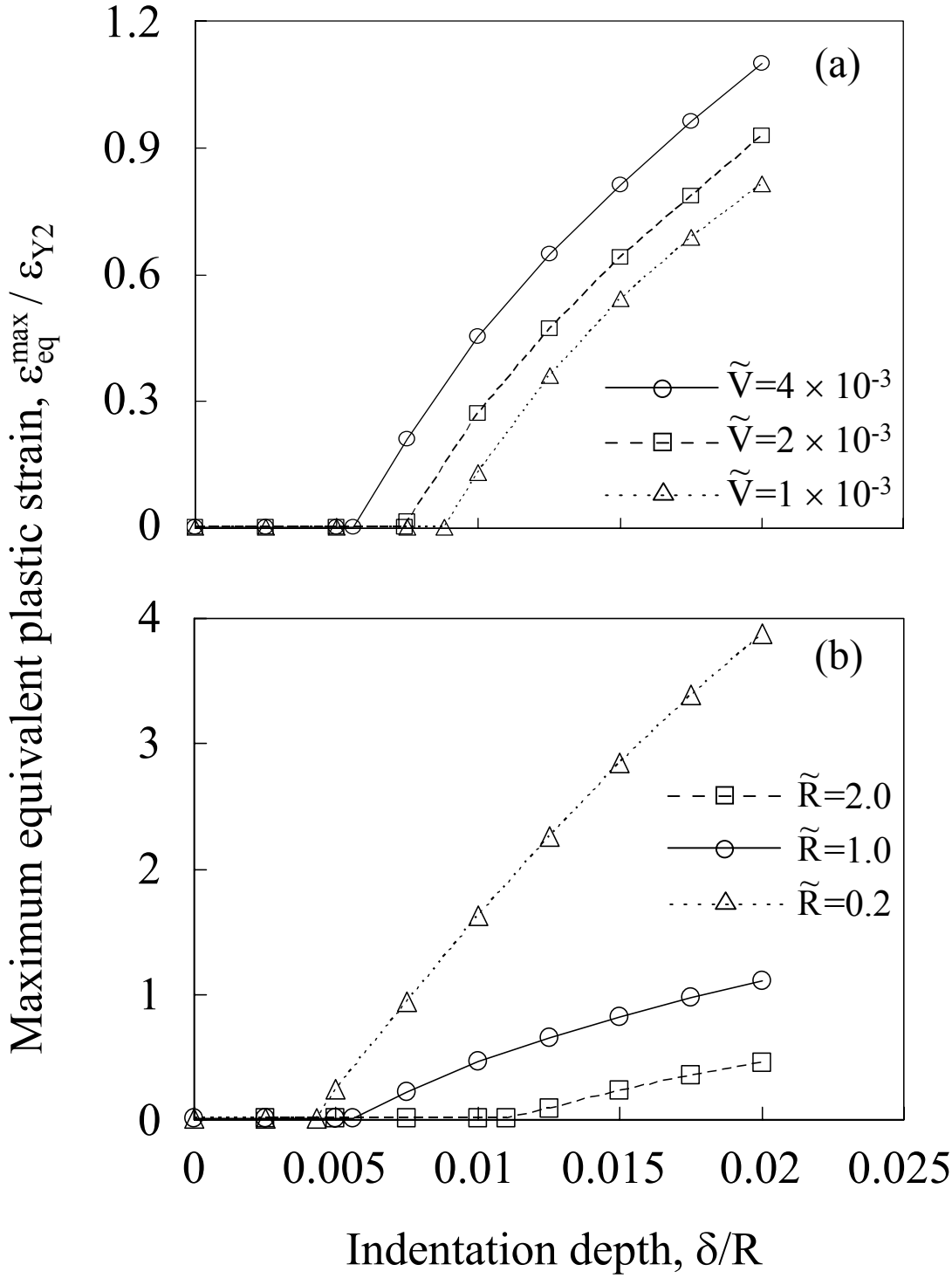
1.2
0.9
0.6
0.3
0
(a)
$\tilde{V}$=4 × 10^{-3}
$\tilde{V}$=2 × 10^{-3}
$\tilde{V}$=1 × 10^{-3}
4
3
2
1
0
(b)
$\tilde{R}$=2.0
$\tilde{R}$=1.0
$\tilde{R}$=0.2
0
0.005
0.01
0.015
0.02
0.025
Maximum equivalent plastic strain, ε_{eq}^{max} / ε_{Y2}
Indentation depth, δ/R

Fig. 14

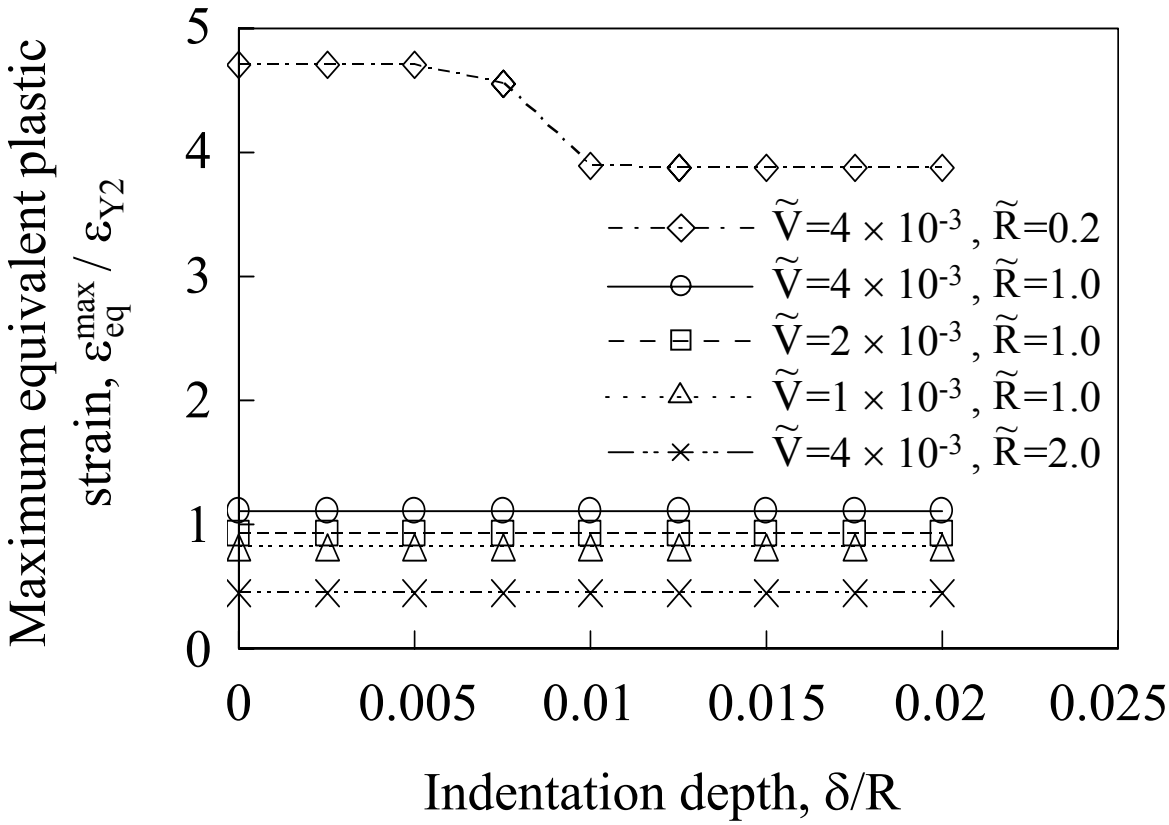
Maximum equivalent plastic strain, $\varepsilon_{eq}^{max} / \varepsilon_{Y2}$
5
4
3
2
1
0
0
0.005
0.01
0.015
0.02
0.025
Indentation depth, δ/R
$\tilde{V}=4 \times 10^{-3}$, $\tilde{R}=0.2$
$\tilde{V}=4 \times 10^{-3}$, $\tilde{R}=1.0$
$\tilde{V}=2 \times 10^{-3}$, $\tilde{R}=1.0$
$\tilde{V}=1 \times 10^{-3}$, $\tilde{R}=1.0$
$\tilde{V}=4 \times 10^{-3}$, $\tilde{R}=2.0$

Fig. 15

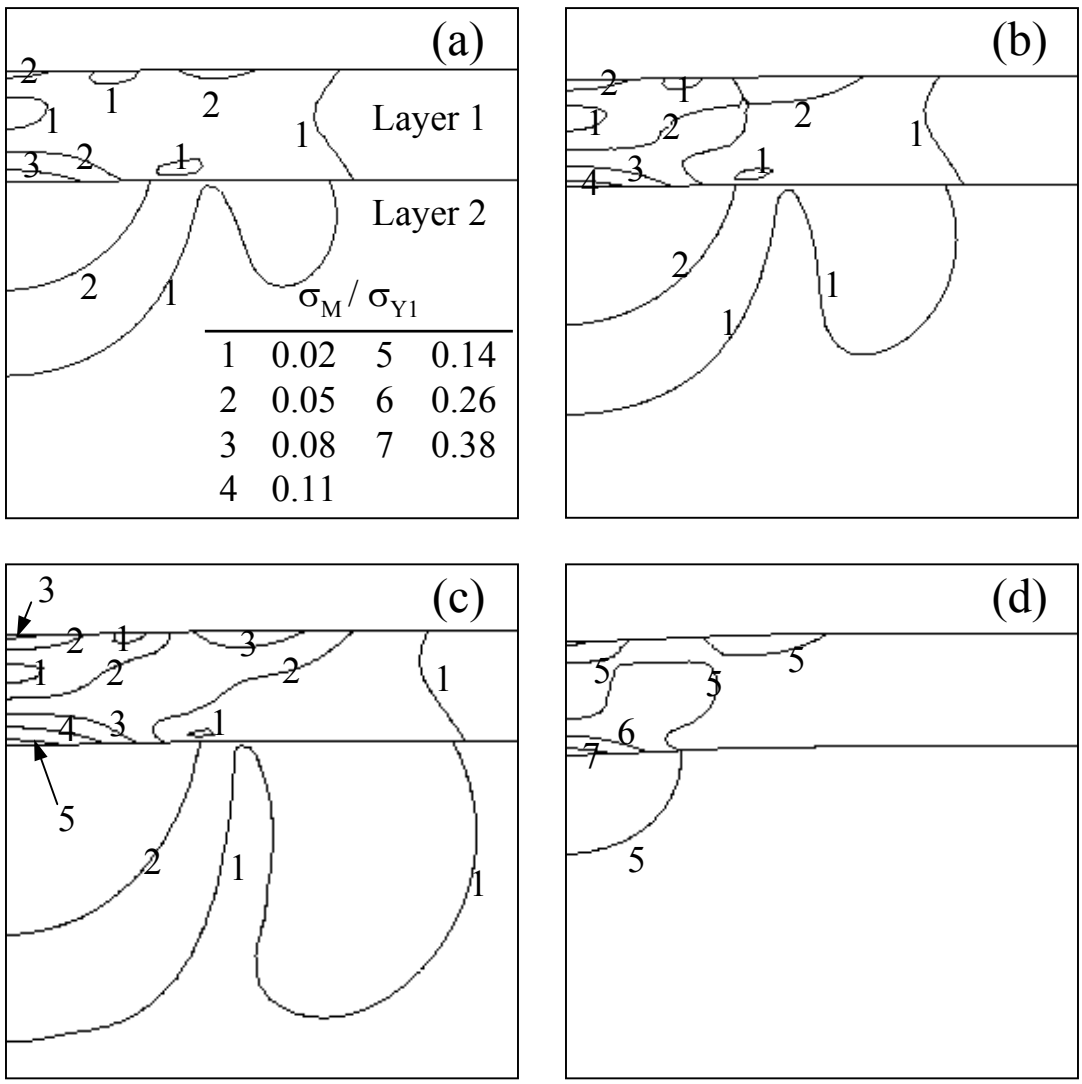
(a)
Layer 1
Layer 2
σ_M / σ_{Y1}
1 0.02 5 0.14
2 0.05 6 0.26
3 0.08 7 0.38
4 0.11
(b)
(c)
(d)

Fig. 16

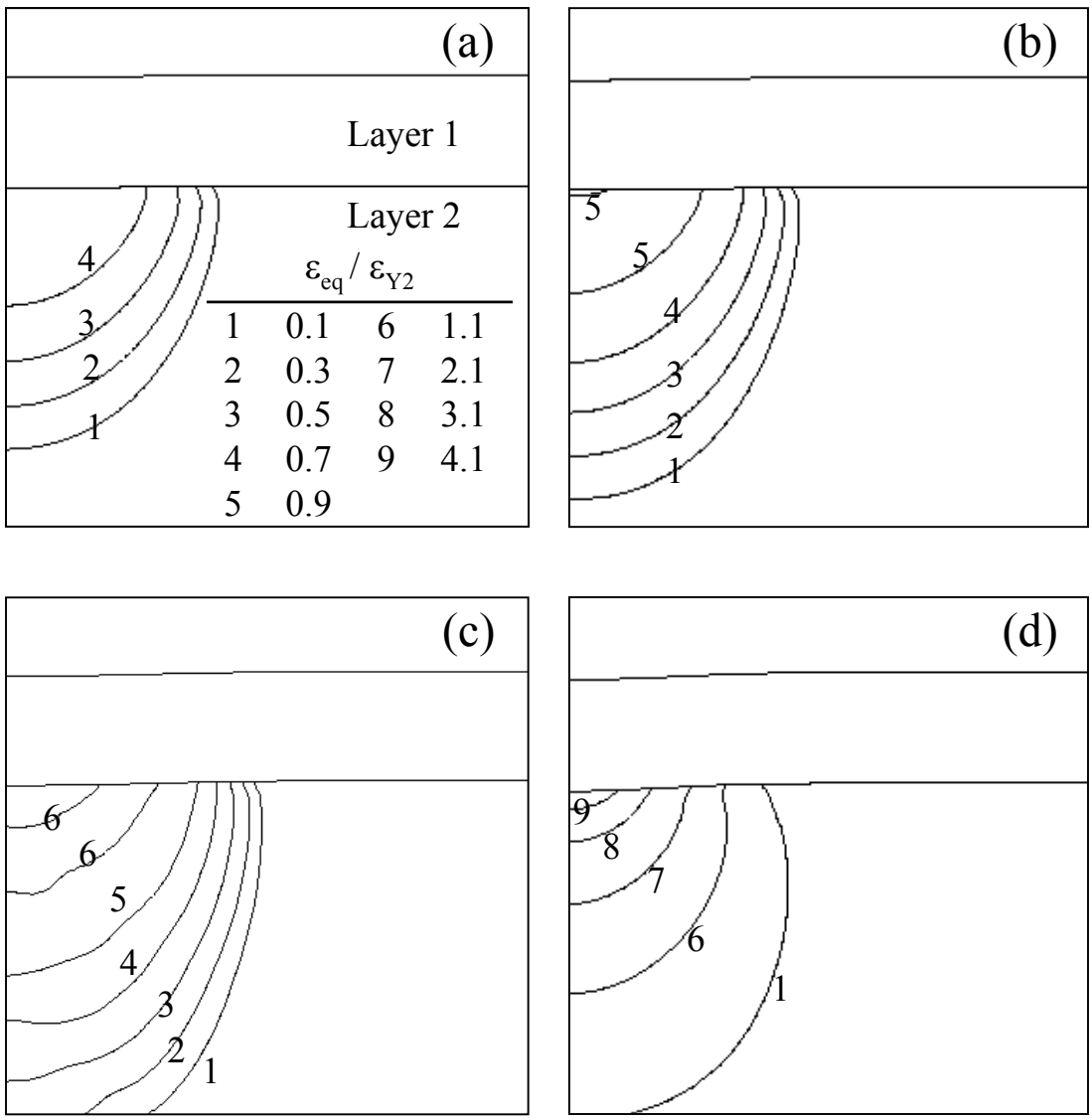
(a)
Layer 1
Layer 2
$\varepsilon_{eq} / \varepsilon_{Y2}$
1 0.1 6 1.1
2 0.3 7 2.1
3 0.5 8 3.1
4 0.7 9 4.1
5 0.9
4
3
2
1
(b)
5
5
4
3
2
1
(c)
6
6
5
4
3
2
1
(d)
9
8
7
6
1

Fig. 17